

*Close to final
revised version : July 2019*

REDUCING SYSTEMATIC DOME ERRORS IN DIGITAL ELEVATION MODELS THROUGH BETTER UAV FLIGHT DESIGN

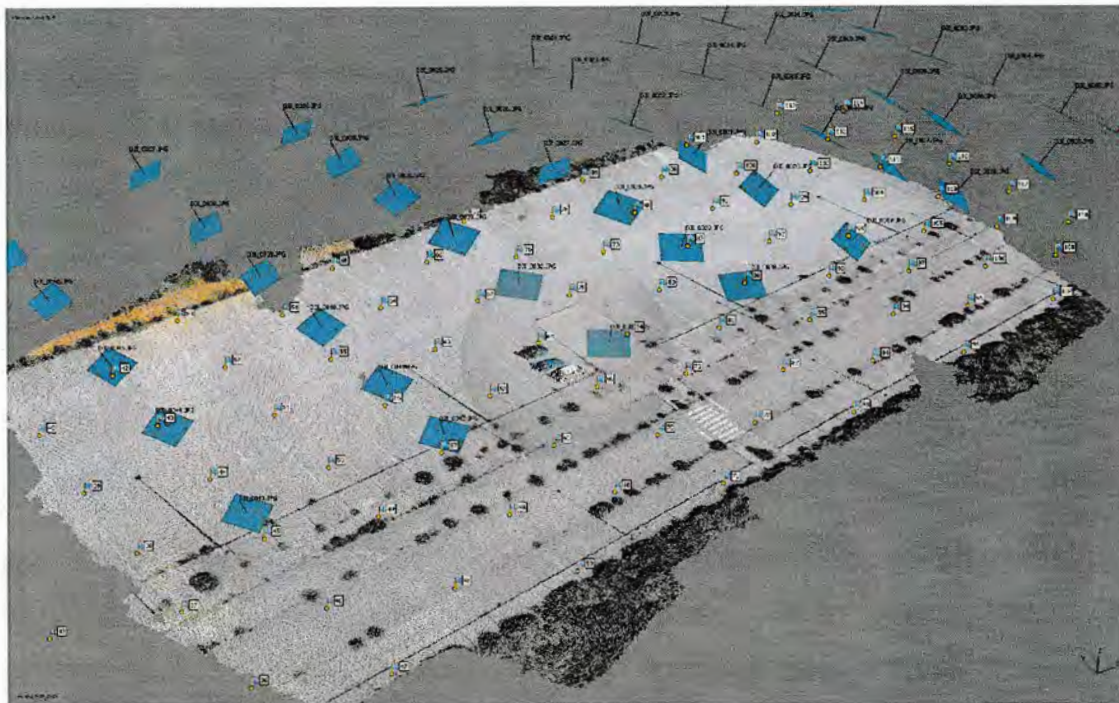
Enoc Sanz-Ablanedo^{*1}, Jim H. Chandler², Pablo Ballesteros-Pérez³, José Ramón Rodríguez-Pérez¹

1 Universidad de León. Grupo de Investigación en Geomática e Ingeniería Cartográfica (GEOINCA). Universidad de León, Avenida de Astorga, sn, 24400, Ponferrada (León), España. Email: enocsanz@unileon.es

2 Loughborough University. School of Architecture, Building and Civil Engineering. LE11 3TU Loughborough, United Kingdom

3 Universidad de Cádiz. Departamento de Ingeniería Mecánica y Diseño Industrial. Escuela Superior de Ingeniería. Campus Universitario, 11519, Puerto Real (Cádiz)

VISUAL ABSTRACT



ABSTRACT

It is well established that Digital Elevation Models (DEMs) derived from Unmanned Aerial Vehicle (UAV) images and processed by Structure from Motion (SfM) may contain important

systematic vertical errors arising from limitations in real camera geometry modelling. Even when significant, such “dome” shaped errors can often remain unnoticed unless specific checks are conducted. Previous methods used to reduce these errors have involved: the addition of convergent images to supplement traditional vertical datasets, the usage of a higher number of Ground Control Points, precise direct georeferencing techniques (RTK/PPK) or more refined camera pre-calibration.

This study confirms that specific UAV flight designs can significantly reduce dome errors, particularly those which increase the number of long distance tie points connecting images and hence the strength of the photogrammetric network. A range of 22 flight designs were tested, including vertical, convergent, point of interest (POI), multiscale and mixed imagery. Flights were carried out over a $300 \times 70 \text{ m}^2$ test field area where 143 ground points were accurately established. Three different UAVs and two commercial software packages were trialled, totalling 396 different tests. POI flight designs generated the smallest systematic errors. In contrast, vertical flight designs suffered from larger dome errors; unfortunately, a configuration that is ubiquitous and most often used. By using the POI flight design, the accuracy of DEMs will improve without the need to use more ground control or expensive RTK/PPK-Systems. The improvement is especially important in self-calibration projects without (or with few) ground control points *open flat terrain* but it is also noticeable when camera pre-calibration is used or when a high amount of ground control is used.

KEYWORDS

DEM, DTM, SfM, UAV flight design, “dome” error

INTRODUCTION

Earth surface mapping with Unmanned Aerial Vehicle (UAVs) has now become a simple and convenient tool for a range of diverse and an ever-increasing range of applications. Two factors have caused the rapid adoption of this technology: the increasingly lower prices of sophisticated camera-equipped UAVs and the emergence of user-friendly Structure from Motion (SfM) photogrammetry software (Turner et al., 2012). Therefore, from cultural heritage surveying or crop inspection to mining pit measurement, the use of these technologies has become common and an increasing number of new users are using such approaches. Whilst the aims or objectives of each application can be very different, all aspire to produce high

quality cartography products, including: 3D visual models, Digital Elevation Models (DEMs) or orthophotos.

The accuracy of an UAV-SfM survey or an UAV 3D model is a complex function of many variables including: camera/ photo quality, image-processing SfM algorithms, camera calibration accuracy, geo-referencing strategy and flight design. Usually, only specific equipment (camera, UAV or software) is available, which constrains many of the variables and only georeferencing strategy and flight design can be directly controlled. Georeferencing strategy now requires either the use of expensive, and not always reliable, equipment for direct georeferencing or the use of ground control points (GCPs), which requires time consuming fieldwork and is expensive. Perfecting flight design provides an important opportunity to improve the geometric quality of a UAV-SfM survey and is the focus of this paper.

It has been frequently reported that digital elevation models (DEMs) derived from photogrammetric SfM processing show characteristic systematic errors (e.g. (Rosnell and Honkavaara, 2012; Javernick et al., 2014; Eltner et al., 2016; Carboneau and Dietrich, 2017; Griffiths and Burningham, 2018; Yurtseven, 2019)). These errors are frequently referred to as "doming" or "bowling". Doming or bowling errors are systematic and affect the whole DEM, mainly in its vertical component. Its name is derived from the uniformly convex (dome) or concave (bowl) deformation that DEMs suffer. Dome (or bowl) errors can be bigger than the usual centimetre resolution of SfM-UAV surveys. When errors are very large (in the range of metres), their presence can be identified easily. However, quite frequently, even significant errors can be disguised and hard to perceive because their size is small in relation to the captured topography (Griffiths and Burningham, 2018).

To detect these errors, specific operations must be performed. These can involve comparison with other more accurate DEMs (James et al., 2017) or quantifying errors at independent ground check points (GChP) whose coordinates are known *a priori*. This creates a challenge. More accurate DEMs are rarely available and the provision of sufficient GChPs distributed evenly across the whole site is labour intensive and can be prohibitively costly for large sites. Additionally, even when this extra fieldwork is conducted, there is a temptation to use such ground points for georeferencing and improve the SfM-UAV survey accuracy, rather than to detect dome errors. It is therefore apparent that such dome errors have been overlooked

frequently by the geoscience community (Griffiths and Burningham, 2018), particularly by new and/or inexperienced users.

Previous research has identified that dome errors seem to be associated with ineffective radial distortion correction arising from inaccurate camera calibration (Fryer and Mitchell, 1987; Wackrow and Chandler, 2008, 2011; James and Robson, 2014; Eltner and Schneider, 2015; Carboneau and Dietrich, 2017). A camera calibration procedure is a computational optimisation involving a mathematical model that attempts to recreate the actual path of the light rays travelling through the camera lenses. Generally, between 6 to 12 parameters are used in an established calibration model based on the pinhole camera (Brown, 1971; Heikkila and Silven, 1997). These parameters are estimated during the Bundle-Adjustment (BA) stage of a normal SfM pipeline (self-calibration) or calculated using imagery captured specifically for calibration purposes (pre-calibration), also with a BA. The better the parameter estimation, the more accurate is the mathematical model used to transform terrain points to image coordinates, and consequently this should minimise any remaining systematic errors. However, it is impossible to model the actual light ray paths exactly. Light rays enter the sensor through a moving hole in 3D space with dimensions of a few millimetres, rather than the fixed and finite point that is assumed in most models. Once inside the camera, light rays must pass through several lenses of varying shape, thickness and refractive indices. These uncertainties cause the actual paths to differ from the straight line assumed by the fundamental mathematical model, collinearity (DeWitt and Wolf, 2000). Hence, despite the use of radial, decentring and other parameters to model the model light paths, a perfect camera calibration is never possible. This means that every photogrammetric 3D model will suffer from uncompensated systematic errors to some extent, the objective being to minimise their effect.

Vertical images (also known as nadir or parallel-axes datasets), have always been considered an efficient way of acquiring aerial images for mapping the Earth surface using traditional photogrammetry (DeWitt and Wolf, 2000). Such images have a similar scale across the whole surface, both shadows and hidden areas (dead ground) are minimized, and so vertical imagery is the best source for orthophoto creation. However, vertical imagery have ~~provides a weak geometric configuration in photogrammetry, particularly over flat terrain, and is usually been considered as a photogrammetric weak geometry prone to doming~~ ^{had} (Wackrow and Chandler, 2008; James and Robson, 2014; Eltner and Schneider, 2015; Carboneau and Dietrich, 2017). In classical manned photogrammetry, and also in some UAV based

surveys (Harwin et al., 2015; Griffiths and Burningham, 2018), the traditional approach to avoid doming has been the use of pre-calibrated metric cameras. However, most small UAVs use small cameras that usually are not designed for photogrammetric purposes. These cameras can have low geometric stability so that their internal elements can slightly move when the camera is manipulated or after on/off/exposure cycles (Shortis et al., 2006; Fraser and Al-Ajlouni, 2006; Sanz-Ablanedo et al., 2010). In such situations, pre-calibration is not useful and the preferred approach is self-calibration (Brown, 1971; Remondino and Fraser, 2006). Unfortunately, if self-calibration is attempted when the photogrammetric network is inherently weak, such as a set of parallel-axes images acquired in a typical vertical block, their determination can be inaccurate and large dome errors are likely to appear (James et al., 2017).

To improve camera self-calibration, convergent images can be integrated with vertical image datasets (Granshaw, 1980; Wackrow and Chandler, 2008; Harwin et al., 2015; Smith and Vericat, 2015; Nesbit and Hugenholtz, 2019). Other recommendations to ensure successful self-calibration in UAV-SfM surveys includes maximising image scale variation within and between images (Fonstad et al., 2013) and utilization of roll angle variation (Fraser, 2018). Although improvements have been successfully demonstrated both in close-range photogrammetry studies (Remondino and Fraser, 2006), laboratory (Wackrow and Chandler, 2011) and through camera perturbation analysis (James and Robson, 2014; Carbonneau and Dietrich, 2017), or photogrammetric network simulation (Dall'Asta et al., 2015) there is limited empirical evidence about the quantitative improvement in UAV-SfM surveys.

to develop parallel processing
camera perturbation
photogrammetric network

The use of Ground Control Points (GCPs) can also improve camera self-calibration and reduce the magnitude of dome errors (James and Robson, 2014; Harwin et al., 2015; James et al., 2017). In general, the higher the number of GCPs, the better the self-calibration (DeWitt and Wolf, 2000; Agüera-Vega et al., 2017; Sanz-Ablanedo et al., 2018). The problem with establishing a dense net of GCPs are the high labour costs involved. For this reason, precise direct georeferencing involving RTK/PPK/PPP systems has emerged as an apparently suitable alternative (Stempfhuber and Buchholz, 2011; Turner et al., 2014; Grayson et al., 2018). This technique uses highly specialized equipment on board the UAV to accurately measure the position of the camera when photos are acquired. The downside of these technologies remains the higher price of the equipment, but also the lack of precise synchronization between camera triggering and the Global Navigation Satellite System

(GNSS) receiver, unexpected loss of resolved ambiguities and the obvious impossibility of measuring several positional epochs at all exact photo positions.

The work described in this study demonstrate that an optimized flight design in which all images are oriented to the centre of the surveyed area, can effectively reduce systematic errors of UAV-SfM surveys. At the same time, the widely used emphasis upon blocks of vertical or nadir images is questioned, regardless whether these are merged with other images types. A wide range of 22 different flight designs has been tested by using 3 different bundle adjustment approaches, including: self-calibration, GCP controlled and pre-calibration. Quality evaluation of derived 3D models is checked by using an extensive and dense network of 143 ground points accurately measured. Three repetitions with three different UAVs were tested, totalling 396 different projects.

MATERIALS AND METHODS

In this section, details will be provided about the equipment used, the nature of the test area and essential information on the tested flight designs.

Equipment

This study used 3 different *DJI phantom 4 Pro* UAVs, to acquire photos of a large test field area. The DJI Phantom 4 Pro is a simple, yet robust, multirotor UAV with 4 motors and a 30-minute flight duration. It weighs 1388 g, including battery and propellers. It is commercial equipment primarily designed for amateur video and photography capture but is frequently adopted for research purposes due its high performance and low price. This specific UAV has also been used in a range of photogrammetry studies (e.g. (Alidoost and Arefi, 2017; Ding et al., 2017; Wang et al., 2017)).

The DJI Phantom 4 Pro incorporates an RGB camera model DJI FC6310. The camera sensor is based on CMOS technology with a physical sensor-size of 13.2x8.8mm, which can generate a 20-megapixel jpg image with a resolution of 5472 columns and 3648 rows. The camera-lens assembly has an approximate focal length of 8.8mm and a mechanical shutter feature that avoids typical rolling shutter problems. The camera is also capable of saving RAW information in DGN files, although this feature was not used in this study. Furthermore, the camera also features a manual exposure option, although the only automatic exposure

was used here. The UAV positioning system uses a code-based single frequency L1 GNSS receiver, which can achieve, according to the manufacturer's specifications, accuracies of 2.5 metres. After each flight, all image files have an approximate geographic location stored in the EXIF header (image: "Properties/Details") derived from this GNSS receiver. However, these locations were not used during the tests described here.

Test area

Flights were conducted on a 300 m by 70 m rectangular flat car park area located in an undeveloped industrial state near Cubillos del Sil, Spain (Latitude 42.63°N; Longitude 6.60°W). On the ground, 143 targets were distributed regularly according to a triangular grid structure (Figure 1). Each target consisted of two circles painted using white paint sprayed onto a CD-ROM placed temporarily on the asphalt to act as a mask. The inner white circle had a diameter of 1.5 cm, whereas the outer circle diameter was 12 cm. A 1.5 m pole with a mini-prism was used to accurately measure the coordinates using a Trimble VX Total Station. According to the manufacturer, this model has an angular accuracy of 1" and a distance accuracy of 1mm+2ppm. Hence, a theoretical relative vertical and horizontal accuracy better than ± 2 mm was achieved for each target. A single Total Station was used for measuring all targets during one single survey session.

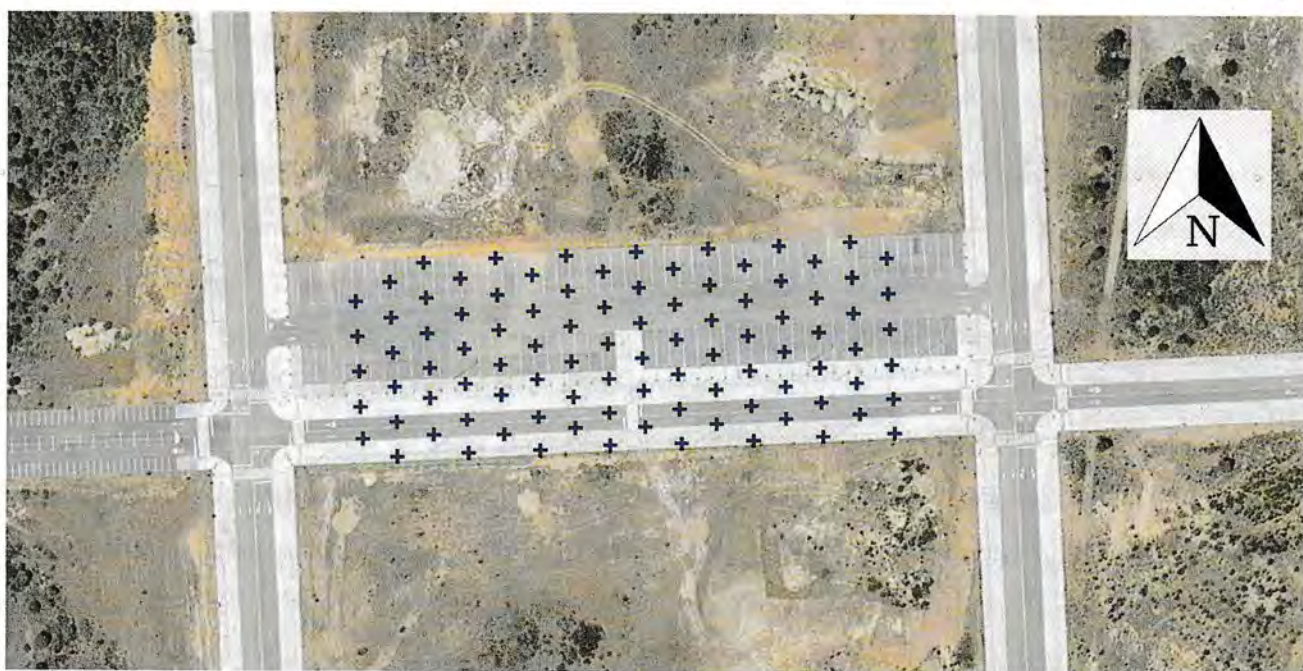


Figure 1. Distribution of Ground Points on the test field area.

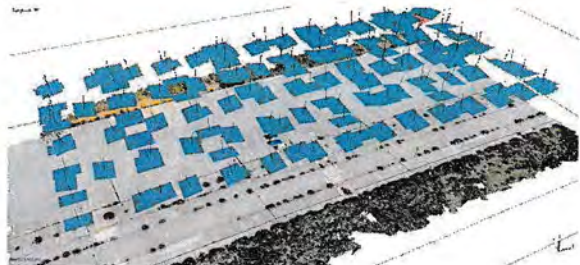
It is worth emphasising that ground points with known coordinates were not used in the bundle adjustment for the self-calibration and pre-calibration approaches. Here, their use was restricted to translating, rotating and scaling the derived rigid 3D model through a single 7 parameter similarity transformation and to provide independent accuracy checks. In the GCP controlled tests the GCP positions were used in the bundle adjustment to establish the relative position and attitude of cameras.

Flight design

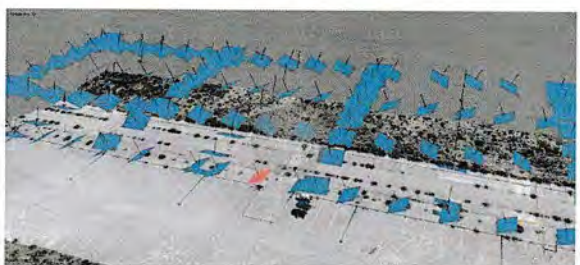
The interest area covered by each flight was located around the centre of the test area. Mission planning was done by the PIX4D Capture App running IOS on an Apple iPad device. This software automatically calculates the photo positions and waypoints, transmitting them to the UAV once the interest area is delimited and the flight height and overlaps specified.

Four different types of image geometries were acquired during different flights: Near vertical, Convergent, Point of Interest and High Altitude. Figure 2 conveys the geometry and the corresponding strips and waypoint positions. In the Near Vertical (a) and High Altitude (d) datasets, photos were taken parallel to the horizontal plane with a maximum of 10° off nadir deviations. In the Convergent datasets, (b) photos were taken at a fixed 25° from the nadir, and as strips were flown in opposing directions, a locally convergent image geometry was achieved. Finally, all Point of Interest (POI) photos (c) had a varying range of angles relative to the nadir, as they always pointed towards the centre of the interest area at ground level.

The near Vertical, Convergent and POI datasets involved 2 different directions, approximately North-South and East-West. The High-Altitude Dataset was oriented East-West only, along the main direction of the test field because of the long base distance between photos. All single strips were programmed with 65% overlap and 45% sidelap (note that when different imageries or crossed strips are ~~mixed~~^{merged} together effective overlaps are much higher). Flight altitudes relative to the ground were similar in almost all flights, with an average of 35 m (Near Vertical), 45 m (Convergent), 40 m (POI). High Altitude flights were captured at 65 m altitude. The corresponding Ground Sampling Distances (GSD) of the different flights ranged between 0.8 and 1.75 cm. Each flight plan (4) was flown by each DJI Phantom Pro unit (3), resulting in 12 datasets. *topic*



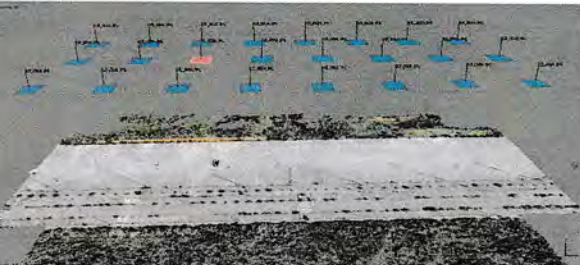
(a)



(b)



(c)



(d)

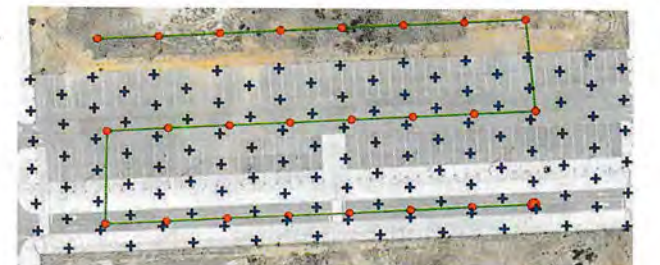
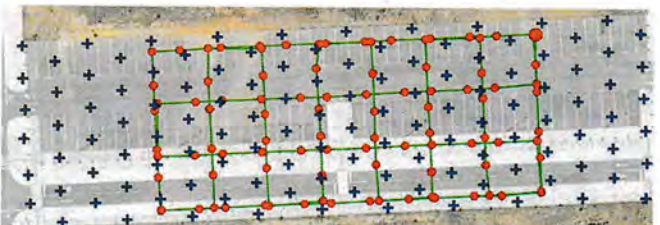
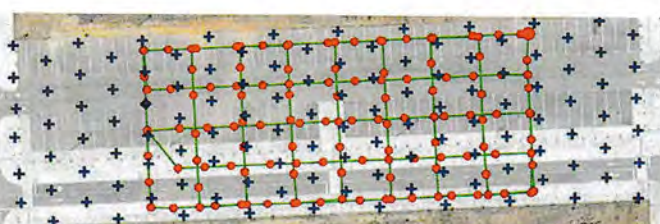
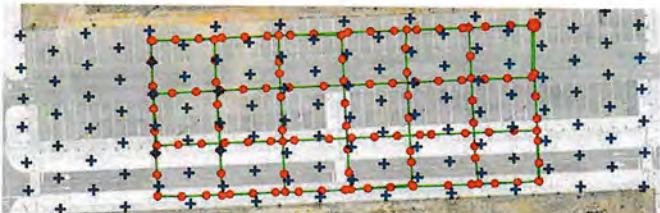


Figure 2. Image geometry and location of waypoints (red circles) and strips (green lines) for the 4 datasets: (a) Near Vertical, (b) Convergent, (c) Point of Interest, and (d) High Altitude datasets. For simplicity, only N-S strips have been included in the Point of Interest 3D visualisation.

Every target appearing in every photo was manually measured on the computer screen. By using the photos in a range of combinations using the 4 different image datasets, a total of 22 different flight designs were tested, each repeated on three occasions. Table 1 shows the number of photos involved and the important characteristics of each combination.

Table 1. Summary of the 22 flight designs used in tests.

ID	Strip Azimuth	Image Datasets Used	Number of images		
			Rep.1	Rep.2	Rep.3
T01	N-S	Near Vertical (NV)	61	62	63
T02	E-W		70	69	68
T03	N-S & E-W		131	131	131
T04	N-S	Convergent (Cnv)	56	57	55
T05	E-W		67	66	67
T06	N-S & E-W		123	123	122
T07	N-S	Point of Interest (POI)	48	47	48
T08	E-W		47	48	47
T09	N-S & E-W		95	95	95
T10	N-S	Close to Vertical + High Altitude (NV + HA)	85	86	87
T11	E-W		94	93	92
T12	N-S & E-W		155	155	155
T13	N-S	Convergent + High Altitude (Cnv + HA)	80	81	79
T14	E-W		91	90	91
T15	N-S & E-W		147	147	146
T16	N-S	Point of Interest + High Altitude (POI + HA)	72	71	72
T17	E-W		71	72	71
T18	N-S & E-W	HA)	119	119	119
T19	N-S & N-S		117	119	118
T20	E-W & N-S	Near Vertical + Convergent (NV + Cnv)	126	126	123
T21	N-S & E-W		128	128	130
T22	E-W & E-W		137	135	135

Three different SfM methodologies were studied: self-calibration, GCP controlled and pre-calibration. In self-calibration, only automatically matched tie points were used in the bundle adjustment for calibrating the camera and for calculating the relative orientation between photos. Ground points were only used for calculating the absolute exterior orientation by applying a rigid similarity transformation. In the GCP controlled tests, all ground points along with automatically matched tie points were used for relative orientation, calibration of camera and exterior orientation. All camera calibration datasets were saved for use in the pre-calibration tests. Optimum calibration parameter sets for each camera were identified by those achieving the lowest ground point residuals. In pre-calibration tests, the best available camera calibration parameters set from previous tests were fixed prior to the bundle adjustment and only automatically matched tie points were used for calculating the relative

orientation between photos. In these final tests, GCPs were only used for calculating the exterior orientation through a rigid similarity transform involving one scale parameter.

Two different commercial software packages were used to process all projects: PhotoScan Pro v1.4.2 and Agisoft Pix4D v4.2.27, to ensure that findings were not software specific. Both packages are commonly used by the SfM scientific community (e.g. (Barbasiewicz et al., 2018; Benassi et al., 2017; Burns and Delparte, 2017; Firdaus and Rau, 2017)). In total therefore, 132 self-calibration, 132 GCP controlled and 132 pre-calibration projects were processed (Table 2).

Table 2. Summary of the projects tested in this study.

Test Type	Software	Repetition	Tested Projects
Self-Calibration	PhotoScan Pro	# 1	22
		# 2	22
		# 3	22
	Pix 4D	# 1	22
		# 2	22
		# 3	22
Ground Control Points	PhotoScan Pro	# 1	22
		# 2	22
		# 3	22
	Pix 4D	# 1	22
		# 2	22
		# 3	22
Pre-Calibration	PhotoScan Pro	# 1	22
		# 2	22
		# 3	22
	Pix4D	# 1	22
		# 2	22
		# 3	22
Total number of projects:			396

With the PhotoScan software, high accuracy, generic preselection and adaptive camera model fitting (only in self-calibration and Ground Control Points Usage) options were used during the bundle adjustment. An upper limit of 40,000 feature points and 4,000 tie points per image was also selected. The same XML file containing ground control information and photo measurements was imported for each project. In Pix4D, all default settings associated with the “Standard 3D maps” template were used. The same XML file previously used with PhotoScan, containing GCPs information and photo measurements was again applied to all

projects. In self-calibration and pre-calibrations tests, calculated coordinates from the GCPs were exported and a 3D similarity transformation was again achieved using in-house developed software. Finally, in both software solutions, the XYZ errors at Ground Control Points were recovered, demonstrating that the Z mean error exceeded the XY mean error by the order of one magnitude.

Figure 3 illustrates four typical graphical representations of the vertical errors found, with gridding obtained using a Minimum Curvature algorithm. (a) shows a project with large Z errors. (b) and (d) show examples of projects with medium to small Z errors. Finally, (e) shows vertical error in a project with very low Z - errors. As expected, both domes and bowls were generated in the results.

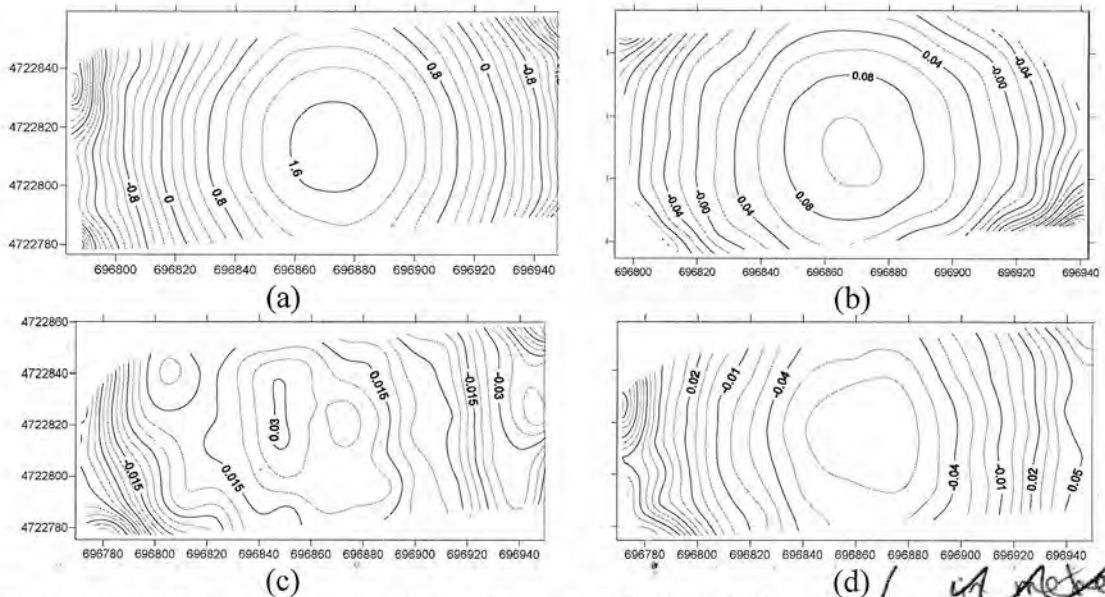


Figure 3. Graphical representation of several dome/bowl errors; (a) One of the larger domes, (b) a small dome, (c) a less evident dome or bowl, and (d) small bowl error.
(ETRS89 UTM H29 reference system).

contour values expressed
in metres

Systematic and random error

In order to exclude random errors from the analysis, Z errors were fitted to a second degree polynomial surface with the Curve Fitting Matlab App. Dome (or bowl) size was calculated as the value of the adjusted surface at the centre of the test field minus the value of the surface evaluated at the corners. When the value of the surface at the centre was greater than the values achieved at the corners, the surface was identified as a dome. Otherwise, errors were

identified as a bowl. All raw XYZ errors, dome height estimations, their precisions and goodness of fit can be found in the additional data files available.

RESULTS

Self-calibration

Table 3 quantifies the dome/bowl sizes for all 132 self-calibration projects, indicating when domes (+ sign) or bowls (- sign) were generated. Here, domes indicate that in the central interest area, photogrammetrically calculated elevations were above the actual Z measured coordinates of GChPs. The opposite happened towards the periphery, where the photogrammetrically calculated elevations were below the actual GChPs heights. Conversely, the minus sign indicates that in the central area, the calculated elevations were below the actual Z measured coordinates of GChPs, whereas in the periphery the errors were positive.

Table 3. Dome/bowl sizes obtained for the 132 self-calibration tests where "+" indicates dome and "-" a bowl shape. Colours have been assigned to help visualize results more clearly. The deepest red cells represent the greater dome/bowl size, whilst the darker blue corresponds to the lowest. White cells represent intermediate error values.

Test #	Strip Azimuth	Image Type	Images #	Dome/bowl size (m) and shape								Average	
				Rep 1		Rep 2		Rep 3					
				MS	Pix4D	MS	Pix4D	MS		MS	Pix4D		
T01	N-S	Near Vertical (NV)	62	1.27	+	1.61	+	4.79	+	4.18	+	0.04	
T02	E-W		69	1.36	+	1.63	+	2.33	+	2.10	+	0.16	
T03	N-S & E-W		131	1.79	+	1.75	+	5.57	+	4.59	+	0.71	
T04	N-S	Convergent (Cnv)	56	0.46	+	0.48	+	0.57	+	0.71	+	0.11	
T05	E-W		67	0.45	+	0.54	+	0.59	+	0.68	+	0.07	
T06	N-S & E-W		123	0.31	+	0.28	+	0.34	+	0.35	+	0.07	
T07	N-S	Point of Interest - (POI)	48	0.21	+	0.46	+	0.32	+	0.41	+	0.02	
T08	E-W		47	0.16	+	0.37	+	0.28	+	0.33	+	0.05	
T09	N-S & E-W		95	0.29	+	0.27	+	0.33	+	0.37	+	0.05	
T10	N-S	Near Vertical + High Altitude (NV+HA)	86	1.47	+	1.96	+	0.21	-	4.30	+	0.94	
T11	E-W		93	1.73	+	2.12	+	0.55	+	2.18	+	1.07	
T12	N-S & E-W		155	2.16	+	2.56	+	1.95	+	4.97	+	1.35	
T13	N-S	Convergent + High Altitude (Cnv+HA)	80	2.44	+	2.38	+	1.79	+	0.91	+	1.10	
T14	E-W		91	0.55	+	2.27	+	2.15	+	0.77	+	1.44	
T15	N-S & E-W		147	2.66	+	2.54	+	2.18	+	0.51	+	1.33	
T16	N-S	Point of Interest + High Altitude	72	1.31	+	1.46	+	1.62	+	0.56	+	1.20	
T17	E-W		71	1.21	+	1.42	+	1.72	+	0.59	+	1.26	
T18	N-S & E-W		119	1.47	+	1.48	+	1.77	+	0.54	+	1.09	
T19	N-S & N-S	Near Vertical + Convergent (NV+Cnv)	118	0.01	-	0.03	-	1.48	+	0.98	+	0.30	
T20	E-W & N-S		125	0.04	+	0.08	+	0.17	+	0.21	+	0.36	
T21	N-S & E-W		129	0.04	-	0.00	-	0.92	+	0.99	+	0.11	
T22	E-W & E-W		136	0.04	+	0.08	+	0.04	+	0.08	+	0.02	
												-0.01	

Closer inspection of Table 3 demonstrates that the smallest errors are associated with the Point of Interest combinations, where dome sizes are under 25 cm. In contrast, the largest errors are associated with combinations that included Near Vertical imagery with large domes over 2 m size. The second-best combination was achieved by mixing Near Vertical with Convergent imageries, although in this case results varied.

Contrary to expectations, the inclusion of two perpendicular or crossed strips resulted in higher errors for Near Vertical projects, both with and without High Altitude imagery. However, additional strips were effective in improving results generated using convergent imagery. In this arrangement, crossed strips worked particularly well (suffered lower errors). Marginal improvements were obtained also in Point of Interest. *when crossed strips are included*

The incorporation of High Altitude images did not seem effective when combined with other vertical, POI or convergent image sets, leading to worse results. Finally, increasing the image overlaps by mixing crossed strips only improved results for the convergent imagery, whereas this worsened for the near vertical.

Out of the 132 self-calibration projects, just 9 created a bowl-shaped error, whilst the remaining 123 projects suffered from dome-shaped errors. Bowl-shaped error surfaces were smaller, whilst projects with medium or large errors were always dome-shaped.

Ground Control Point Controlled and Pre-calibration

In addition to the 132 self-calibration projects, new projects were created with identical imagery to check accuracies achieved using two other approaches: GCP controlled and pre-calibration. In the GCP controlled projects, every ground point was used as control during the bundle adjustment. In the pre-calibration approach, the optimum calibration parameter set available was imposed on all projects and no GCPs were used during the bundle adjustment. Table 4 compares the resulting dome/bowl sizes, where each cell is an average of the 3 repetitions. (Note that detailed data for the 396 projects can be consulted by referring to the additional material). Pre-calibration achieved better results than self-calibration, which agrees with the work of Griffiths and Burningham, (2018). However, the best results were achieved when a very dense network involving 143 accurate GCPs was used, achieving much lower domes sizes (0.05 m) than either pre-calibration (0.23 m) and self-calibration projects (0.97 m).

Table 4. Comparison between the accuracies obtained in self-calibration, GCP controlled and pre-calibration for the 396 tests. Each cell is the average of 3 repetitions. (Complete results are provided in additional data). Colours have been assigned to help visualize results more clearly. The deepest red cells represent the greater dome/bowl size, whilst the darker blue correspond to the lowest.

Test #	Strip Azimuth	Image Type	Dome / bowl size (m)			
			Self-Calibration	GCPs Controlled	Pre-Calibration	Average
T01	N-S	Near Vertical (NV)	2.09	0.03	0.62	0.813
T02	E-W		1.30	0.03	0.11	
T03	N-S & E-W		2.60	0.06	0.47	
T04	N-S	Convergent (Cnv)	0.44	0.01	0.13	0.149
T05	E-W		0.40	0.02	0.04	
T06	N-S & E-W		0.24	0.02	0.04	
T07	N-S	Point of Interest (POI)	0.24	0.03	0.08	0.101
T08	E-W		0.22	0.02	0.02	
T09	N-S & E-W		0.22	0.03	0.04	
T10	N-S	Near Vertical + High Altitude (NV+HA)	1.58	0.04	0.84	0.792
T11	E-W		1.30	0.05	0.44	
T12	N-S & E-W		2.31	0.05	0.51	
T13	N-S	Convergent + High Altitude (Cnv+HA)	1.44	0.06	0.42	0.575
T14	E-W		1.21	0.08	0.17	
T15	N-S & E-W		1.56	0.09	0.15	
T16	N-S	Point of Interest + High Altitude (POI+HA)	1.04	0.11	0.18	0.436
T17	E-W		1.05	0.10	0.14	
T18	N-S & E-W		1.07	0.10	0.12	
T19	N-S & N-S	Near Vertical + Convergent (NV+Cnv)	0.48	0.02	0.28	0.082
T20	E-W & N-S		0.18	0.02	0.10	
T21	N-S & E-W		0.37	0.02	0.16	
T22	E-W & E-W		0.05	0.01	0.08	
		Average	0.97	0.05	0.23	

The optimum results in the three georeferencing strategies were obtained in test T22, where combined Near Vertical and Convergent imagery, both in E-W direction, was used. With a simpler setup and less images, all the three POI setups achieved good results. Near to Vertical and Near to Vertical with High Altitude imagery achieved the poorest global results both, in pre-calibration and GCP controlled. Finally, the addition of high altitude imagery always worsened the results of simpler design flights.

For each repetition, a different DJI Phantom 4 Pro was used. Whilst performance between different flights designs were equivalent for the three repetitions, the third repetition showed a globally lower error. Additional checks showed that the 3rd Phantom 4 Pro had newer firmware (v01.07.1641; 1.2.0; v1.0.0) than the 1st and 2nd (v01.06.1610; 1.1.6; v1.0.0). This was the only difference found between the 3 repetitions.

Image Residuals

Image residuals refer here to the global average vector (in pixels) of the reprojection error of all tie points of a project. Tie points are those 3D points derived from the matching and alignment step in the FM pipeline. Reprojection error was calculated by comparing the

computed coordinates of tie points re-projected onto the photos with their measured positions, originally detected by the image matching algorithm.

It may be imagined that inaccurate camera calibration should generate results which exhibit higher residuals or differences between projections of object points onto the images and their associated measured positions. However, Figure 4 below shows that image residuals and object RMSE do not ~~always agree completely~~ ~~agreed~~. It can be seen how the Near Vertical combinations showed the lowest residuals in the images but created some of the highest domes. Also it is possible to observe that flight setups containing High Altitude Imagery generated the highest image residuals.

Test #	Strip Azimuth	Image Type	Dome Size (m)	Residual in Images (px)
T01	N-S	Near Vertical	0.92	0.38
T02	E-W		0.48	0.35
T03	N-S & E-W		1.07	0.49
T04	N-S	Convergent	0.18	0.40
T05	E-W		0.14	0.43
T06	N-S & E-W		0.10	0.49
T07	N-S	Point of Interest - (POI)	0.10	0.48
T08	E-W		0.07	0.46
T09	N-S & E-W		0.10	0.54
T10	N-S	Near Vertical + High Altitude	0.59	0.78
T11	E-W		0.54	0.79
T12	N-S & E-W		0.79	0.90
T13	N-S	Convergent + High Altitude	0.75	0.70
T14	E-W		0.54	0.76
T15	N-S & E-W		0.77	0.82
T16	N-S	Point of Interest + High Altitude	0.56	0.82
T17	E-W		0.54	0.82
T18	N-S & E-W		0.56	0.87
T19	N-S & N-S	Near Vertical + Convergent	0.30	0.54
T20	E-W & N-S		0.10	0.46
T21	N-S & E-W		0.18	0.56
T22	E-W & E-W		0.04	0.47

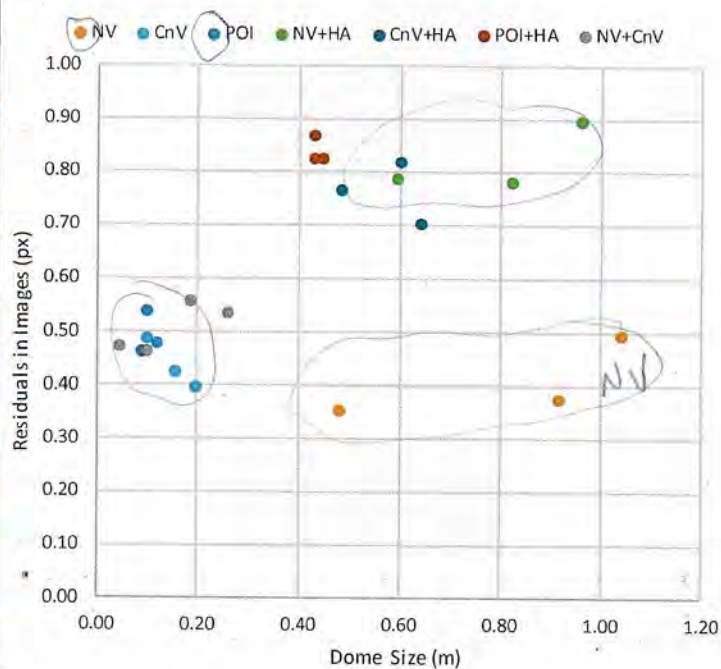


Figure 4. Analysis of global RMSEs in GChPs vs photo residuals. Data has been extracted from the 132 self-calibration tests and averaging the three repetitions. NV is Near Vertical, CnV Convergent, POI Point of interest and HA High Altitude. Colours have been assigned to help visualize results more clearly. The deepest red cells represent the greater dome/bowl size and image residuals, whilst the darker blue corresponds to the lowest.

Software dependence

To ensure that patterns are not software dependent, all data were processed with two different software packages. Figure 5 compares the dome size values as registered after conducting the image processing for each software package. The three repetitions were

averaged and represented as a single point in Figure 5 right, showing a good general agreement between packages. However, PhotoScan appears to perform slightly better in all flight designs, except the Point of interest + High Altitude and Convergent + High Altitude case. This can be perceived easily, as those points remaining below the bisector line in the right-hand plot. Pix4D seems to be better with Near Vertical + High Altitude but PhotoScan was slightly better in CnV + HA and POI + HA. Globally, pix4D achieved an averaged dome sizes of 0.95 m whereas PhotoScan achieves 1.00 m.

PhotoScan

Test #	Strip Azimuth	Image Type	Dome Size (m) MetaShape	Dome Size (m) Pix4D
T01	N-S	Near Vertical (NV)	2.03	2.16
T02	E-W		1.28	1.31
T03	N-S & E-W		2.69	2.52
T04	N-S	Convergent (Cnv)	0.38	0.49
T05	E-W		0.37	0.43
T06	N-S & E-W		0.24	0.24
T07	N-S	Point of Interest (POI)	0.18	0.30
T08	E-W		0.16	0.28
T09	N-S & E-W		0.22	0.23
T10	N-S	Near Vertical + High Altitude (NV+HA)	0.88	2.28
T11	E-W		1.12	1.48
T12	N-S & E-W		1.82	2.81
T13	N-S	Convergent + High Altitude (Cnv+HA)	1.78	1.11
T14	E-W		1.38	1.03
T15	N-S & E-W		2.06	1.06
T16	N-S	Point of Interest + High Altitude (POI+HA)	1.38	0.71
T17	E-W		1.39	0.71
T18	N-S & E-W		1.44	0.70
T19	N-S & N-S	Near Vertical + Convergent (NV+Cnv)	0.59	0.36
T20	E-W & N-S		0.19	0.16
T21	N-S & E-W		0.35	0.38
T22	E-W & E-W		0.03	0.06

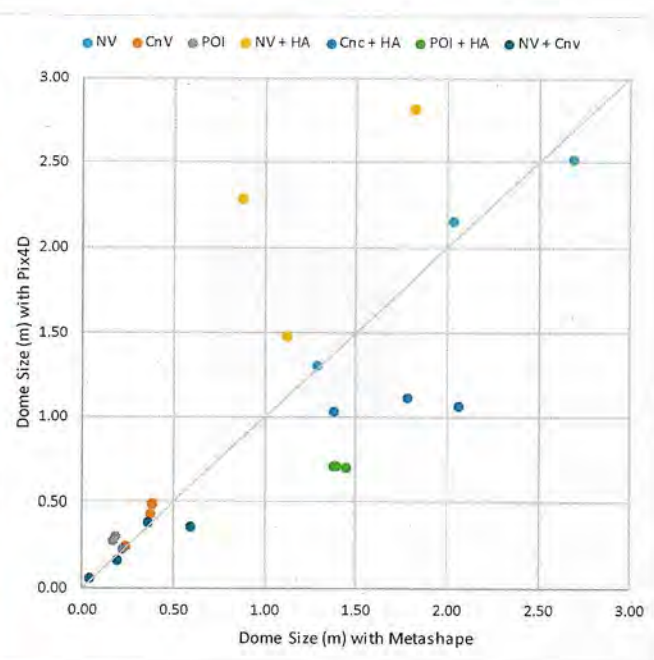


Figure 5. Comparison of RMSE 3D errors obtained by PhotoScan Pro and Agisoft Pix4D. (1:1 line is grey). NV is Near Vertical, CnV Convergent, Pol Point of interest and HA High Altitude. Colours have been assigned to help visualize results more clearly. The deepest red cells represent the greater dome/bowl size, whilst the darker blue corresponds to the lowest.

Dependence of dome size with flight design geometry

In order to understand why the vertical imagery is particularly prone to producing large domes in SfM processing whilst POI works much better, the geometry of ray intersections has been examined. The fifth column (Table 5) shows the number of epipolar intersections arising from each homologous SfM local feature in all the projects for the first repetition. The number of intersections is obviously highly correlated with the number of images (column 6) (Pearson Correlation Coefficient, $r=0.90$) but is not correlated with the dome size ($r=0.13$), the number of intersections per image (column 7) or the number of intersections per 3D tie point (column 8).

8) also are not correlated with dome size ($r=0.04$ and $r=0.09$, respectively), so image overlap doesn't seem to be the key to reducing systematic dome errors. By using a Matlab script (available in additional data files) the angle between the epipolar lines and every tie point intersection was calculated. Figure 6 shows a density histogram for these angles for three flight setups: Near Vertical (NV), Convergent (Cnv) and Point of Interest Imagery (POI); all three computed using single direction strips.

As can be observed, angles arise from several populations corresponding to the epipolar intersections between different strips. For example, the Near Vertical setup has a first peak density maximum with a 20° intersection, which corresponds to consecutive photos in the same strip and a b/h ratio of only 0.35. The second maximum corresponds to intersections between 2 consecutive strips at about 38° (b/h ratio = 0.69). These two populations have a low b/h ratio, involving images that degrade the precision of the intersected coordinates. The maximum precision is achieved when there is an equilateral triangle between the images and the intersection point, which creates an angle of 60° and a b/h ratio = 1.15. Around this convergence ($50-70^\circ$), the POI flight setup has a higher number of intersections (20%) than either NV (10%) or Cnv (14%) flight setups.

The second interesting observation raised by figure 6 is that POI imagery includes 8% of intersections with an angle greater than 80° , and a b/h ratio higher than 1.67. These correspond to images that effectively create links between remote images. At 90° (b/h=2) there is a maximum, indicating that very far strips are connected. This does not occur with NV setup, where the farthest connected strips have a b/h ratio of just 1.4 and most of intersections are under 50° . The final column in Table 5 shows the minimum b/h ratio of the 10% furthest epipolar intersections for every flight setup. A Pearson value of -0.53 between this variable and dome sizes indicates a large inverse effect (Cohen, 1988) between the number of remote image connections and dome mitigation.

Table 5. Analysis of epipolar intersections.

Test #	Strip Azimuth	Image Type	Dome Size (m)	Number of Intersections	Number of Images	Intersections per Image	Intersections per Tie Point	Minimum b/h ratio of furthest 10% intersections
T01	N-S	Near Vertical (NV)	2.09	251 612	61	4 124.8	2.8	2.4
T02	E-W		1.30	291 887	70	4 169.8	2.8	3.5
T03	N-S & E-W		2.60	1 165 151	131	8 894.3	9.7	2.8
T04	N-S	Convergent (Cnv)	0.44	255 865	56	4 569.0	3.3	3.0
T05	E-W		0.40	438 617	67	6 546.5	5.3	4.8
T06	N-S & E-W		0.24	1 339 964	123	10 894.0	12.2	4.2
T07	N-S	Point of Interest (POI)	0.24	295 503	48	6 156.3	4.9	6.6
T08	E-W		0.22	251 747	47	5 356.3	3.9	7.1
T09	N-S & E-W		0.22	1 336 366	95	14 067.0	18.7	7.3
T10	N-S	Near Vertical + High Altitude (NV + HA)	1.58	710 394	85	8 357.6	7.8	2.6
T11	E-W		1.30	794 451	94	8 451.6	7.7	3.0
T12	N-S & E-W		2.31	1 976 230	155	12 749.9	17.2	2.9
T13	N-S	Convergent + High Altitude (Cnv + HA)	1.44	657 021	80	8 212.8	7.6	3.3
T14	E-W		1.21	976 355	91	10 729.2	11.8	4.1
T15	N-S & E-W		1.56	2 184 660	147	14 861.6	21.0	4.2
T16	N-S	Point of Interest + High Altitude (POI + HA)	1.04	768 712	72	10 676.6	11.1	5.4
T17	E-W		1.05	716 572	71	10 092.6	9.7	5.4
T18	N-S & E-W		1.07	2 077 623	119	17 459.0	28.5	6.0
T19	N-S & N-S	Near Vertical + Convergent (NV + Cnv)	0.48	964 487	117	8 243.5	8.2	3.1
T20	E-W & N-S		0.18	1 394 937	126	11 070.9	11.1	3.8
T21	N-S & E-W		0.37	1 306 818	128	10 209.5	11.0	3.8
T22	E-W & E-W		0.05	1 402 563	137	10 237.7	11.1	3.8

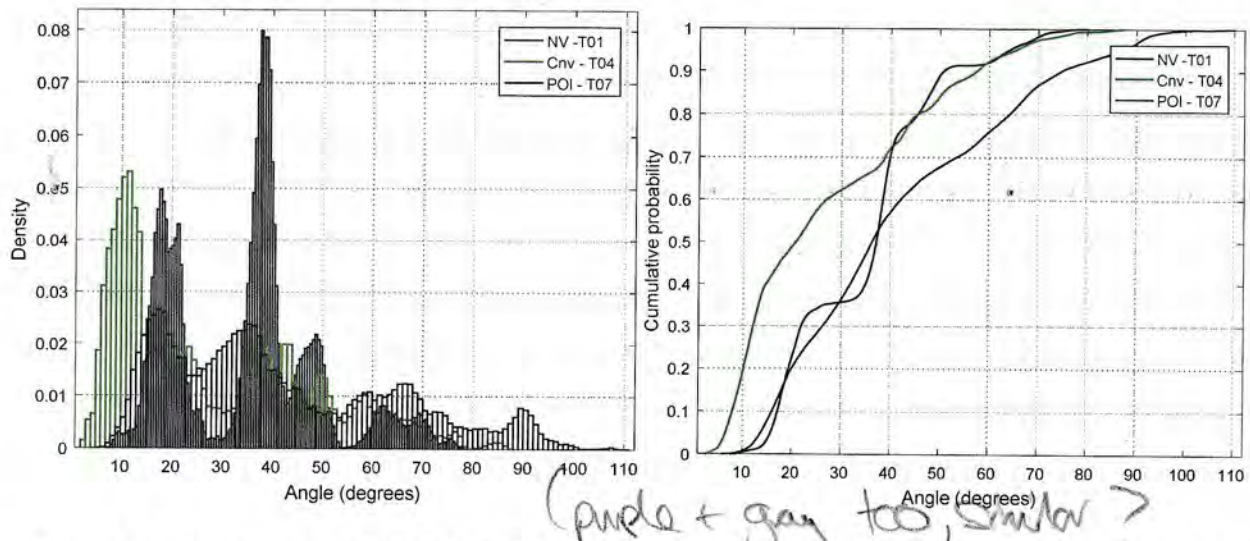


Figure 6. Comparison of RMSE 3D errors obtained by PhotoScan Pro and Agisoft Pix4D. (1:1 line is grey). NV is Near Vertical, Cnv Convergent, Pol Point of interest and HA High Altitude.

DISCUSSION

fall 2018

This study confirms the findings of a range of previous work (Wackrow and Chandler, 2008, 2011; James and Robson, 2014; Woodget et al., 2015; James et al., 2017; Caronneau and Dietrich, 2017) concerning the existence of systematic dome-shape errors that arise from imperfections in camera calibration. In this study, a huge number involving 396 different projects using 22 different flights setups, 3 georeferencing strategies and 3 repetitions has led to a better characterisation of these domes. In most tests performed, a clear dome (convex-shaped) or a bowl (concave-shape) deformation in the 3D model was observed. These errors fit well with a 2nd-degree polynomial surface, which agree with Yurtseven's observations (Yurtseven, 2010). In the absence of a clear dome or bowl, small but highly systematic undulations were still identified. The magnitude of domes was found to be highly significant when expressed in relative terms. With the self-calibration approach involving just near vertical imagery taken at 35m altitude, some domes were greater than 4m, which represents a very poor vertical accuracy. In contrast, the optimum flight designs generated domes sizes of just 0.25m through self-calibration, 0.10m with pre-calibration and 0.02m by using all GCPs. These systematic errors seemed to primarily adopt the shape of a dome rather than a bowl (123 out of 132 in self-calibration). It is significant that those projects affected by large and medium errors always created a "dome" and never a "bowl". The reason why these errors appear preferentially in the form of domes remains uncertain. However, it could be important since it could give clues to the reduction of them using other routes than the one proposed in this work. Simply, as a hypothesis, it is suggested that in the computation of the coordinates of local features during the SfM automatic matching stage, the change of scale from the centre of the image to the edges should be taken into account.

It is well known that the magnitude of dome errors varies by using different UAV multirotor flight designs (James and Robson, 2014; Caronneau and Dietrich, 2017). Traditional practical recommendations normally include the addition of convergent imagery to the traditional vertical datasets. However, our results suggest that a Point of interest (POI) flight design, in which all photos are directed towards the centre of the survey, resulted in the best flight configuration setup. This flight imagery was very effective in mitigating domes in self-calibration tests, both in mixed and non-mixed crossed strips. POI flight design was even effective in pre-calibration tests where all interior camera parameters remained fixed whilst estimating the external orientation parameters. Two different software packages, and three repetitions with different UAVs confirmed these findings. It is suggested therefore that POI designs should be the default option when conducting UAV mapping. This finding is possibly

intuitive to close range photogrammetrists but has not been reported widely before, and at least not supported by full scale tests using a UAV. Nevertheless, the proposed flight setup does have its limitations. If the site area is physically much larger than the relative flight altitude, optical axes will be too oblique at site borders and there will be excessive variation in scale across each photo, causing the overlaps to be reduced towards the block periphery. For large sites, higher altitude POI flights and splitting the project into subsites could provide a solution to this challenge. Sites which are perhaps unsuitable for POI flight geometry are those comprised of ~~linear~~^{long} features, such as rivers or roads.

Unsurprisingly, flight designs containing just vertical images generated larger dome errors and almost always achieved the poorest global results. Mixing crossed strips of vertical images (and then increasing the photographs overlap ratio) did not improve results, even ~~lowering~~^{lower} them occasionally. Adding a second dataset of vertical images acquired at higher elevations was generally not useful either. This poor performance of vertical imagery agreed with previous studies too (e.g. (Fryer and Mitchell, 1987; Wackrow and Chandler, 2008, 2011; Eltner and Schneider, 2015; James et al., 2017; Carboneau and Dietrich, 2017; Nesbit and Hugenholtz, 2019)). In these studies, the addition of convergent imagery ~~is~~ recommended to achieve a stronger photogrammetric network. These recommendations agreed with our results since Near Vertical + Convergent imagery was generally effective in dome mitigation of Near Vertical datasets. However, in our study, merging vertical photos with other datasets generally degraded performance. The problem associated with single vertical image datasets seems to be reproduced in mixed setups, as any benefit from other flight setups seem to disappear when vertical imagery is added.

In this study, a large inverse effect has been found between dome size and the percentage of epipolar intersections with a large b/h ratio. This suggests that distant image connections ~~can help reduce dome size~~ could be the cause of reduction of dome/bowl size. Successive and highly overlapped vertical photos are by definition very similar, with almost the same scale and viewing directions. Arguably, homologous local features in these photos will rank very highly during the automatic matching in the SfM pipeline, achieving low image residuals. Unfortunately, although useful for automatic matching using SIFT or similar based algorithms, the low base/height ratio of adjacent photos creates weak epipolar intersections, which creates uncertainty in the coordinates representing local features. ~~In contrast~~ On the other side, the POI flight design reduces the number of these weak intersections and maximizes the number of optimal

which
angles intersection (60°). ~~This~~ increases the number of image links with long b/h ratios. Interestingly this finding is supported by Fraser (2018) in unpublished work, where it is recommended to "maximise scale variation within & between images" as this minimizes the projective coupling between calibration parameters.

The low performance of vertical imagery is striking, as this type of image configuration has been traditionally considered the most effective to acquire, particularly in terms of shadow reduction, scale homogeneity, coverage efficiency and simplicity. Although these factors remain relevant and help explain its widespread adoption, it is possibly the historical traditions of aerial mapping photogrammetry that are to blame for the persistence of this geometry. Traditionally, metric film cameras equipped with laboratory calibrated and distortion free lenses were used for mapping. Flight designs consisting of vertical images acquired with 60% end-lap and 20% side-lap were universally obtained worldwide for generations of mapmaking, using mainly manual measurement methods (DeWitt and Wolf, 2000). Modern SfM photogrammetry is very different and many of the older justifications for using vertical image sets have lost their value. In SfM photogrammetry, both image capture and subsequent data processing is wholly digital and highly automated, which finally leads to the usage of much higher number of images and higher end-lap and side-lap ratios to prevent shadow areas. UAV flights are completely autonomous and complex designs can be ~~completely~~ automatically executed. Pre-calibration seems not to be the most logical option for modelling the geometry of non-stable, non-metric cameras and self-calibration requires strong photogrammetric networks. All these differences should force the user community to reconsider whether vertical imagery remains desirable for UAV mapping today. Results from this study support the fact that vertical imagery should be avoided whenever possible.

In Point of interest (POI) imagery, which is now the recommended flight geometry, ~~the~~ location of photos is the same as the traditional vertical flight setup. Traditional vertical flight patterns can be easily converted to POI flight setups without losing resolution or without requiring increased flight times. However, the camera is oriented to the centre of the surveying area at each location. Consequently, a very wide of camera angles, scales and convergences are ~~will be~~ achieved ~~when~~ will be favourable not only for dome/bowl reduction but also in terms of reducing shadow areas. Such wide camera angles and ~~convergences~~ provides a strong photogrammetric network that improves camera calibration by avoiding local and non-real (false) solutions in a very highly coupled parameter sets. One limitation of the proposed POI

flight setup is the size of the interest area, which should not be higher than 4-5 times the flight height in order to avoid excessive convergence angles. In these situations, several POI configurations could be flown, each with its own foci.

The two packages used during the tests generated similar results for the different flight designs. This is encouraging because it suggests strongly that the origin of systematic vertical errors previously identified cannot be attributed to specific software. Also, three different DJI Phantom 4 Pro platforms were used. While performance between different flights designs were equivalent for the three repetitions, the unit with a newer firmware showed generally lower RMSE. Although in this study there is insufficient evidence to ensure that different firmware will derive different accuracies, it must be recognised that camera firmware, as those used in the study, try to remove excessive optical distortions through resampling when producing JPG files. It could happen that transformed images have different geometric mathematical deformations than those naturally found in lenses. In such case, it could be hard to model with traditional camera models developed by (Brown, 1971; Heikkila and Silven, 1997). Maybe, photogrammetric practitioners should more routinely use the raw information that is initially produced by the planar sensor and then calibrating the cameras explicitly.

Finally, it has been frequently reported that the use of GCPs reduce dome errors (James and Robson, 2014; James et al., 2017). Our work demonstrate that this is true, with one caveat. If the control is distributed solely around the site periphery in a circular form then, irrespective of their number, they will be ineffective at reducing dome errors. Indeed, minimisation of residuals by the bundle adjustment will ensure that the GCPs will achieve very low RMSE values, as the resulting parameters and the consequent dome will accommodate their existence. To be effective in dome mitigation, GCPs must be distributed homogenously across the whole interest area, preferably in the form of a triangular grid since this layout minimises the distance between any two GCPs. A last cautionary note is that GCPs, even when adequately distributed, are not useful for **detecting** dome/bowl error surfaces if they are used during the bundle adjustment. To detect dome/bowl errors, only GChPs should be used (i.e. points NOT incorporated and constrained during the bundle adjustment).

CONCLUSIONS

It is well known that all UAV 3D models are affected by systematic error surfaces, which can be termed "doming" or "bowling". These errors, which come from inaccurate camera calibration, can be large but often go unnoticed if specific operations to identify and quantify their existence are not performed.

In this work we have demonstrated that the magnitude of these dome errors can be mitigated by using an optimum flight design, in which all images are oriented to the centre of the surveyed area (POI flight setup). Twenty-two different flight designs were tested including vertical, convergent, multiscale, point of interest and mixed imagery. To increase study reliability, the flights were repeated 3 times with different UAVs and processed using 2 different software packages. Results suggest that mitigation of domes/bowls in Point of Interest flight design is achieved due to the increased number of connections between remote images. The POI flight geometry maximises the number of optimal intersection angles (60°) and consequently reduces the number of weak intersections with low b/h ratios.

Flight designs including only vertical imagery, which have the lowest number of distant connections, showed the poorest results. When this vertical imagery is mixed with other flight designs, only intermediate results are obtained. Indeed, increasing the vertical photo overlaps and by mixing a higher number of vertical crossed images or adding higher altitude vertical imagery does not improve results either, so no supporting justification or benefits for using vertical imagery was found. All these differences should force the user community to reconsider whether vertical imagery remains appropriate for UAV mapping today. Results from this study support the fact that vertical imagery should be avoided whenever possible.

One limitation of the proposed POI flight setup compared with the widely used vertical images block is the size of the interest area. It should not be higher than 4-5 times the flying height to avoid excessive convergence angles. In these situations, several POI flights with multiple foci could be captured.

The main beneficiaries of this study will be environmental researchers planning to use multirotor UAVs to obtain digital elevation or terrain models, particularly if there is insufficient time or resource for an intensive campaign to establish ground points, either for control or checks. The optimum benefit from the proposed method, in the form of a high-quality georeferenced model, will be achieved by using just three GCPs for absolute georeferencing.

Of course, this flight design is compatible with alternative methods of dome mitigation, such as pre-calibration, RTK/PPK flights, or dense GCPs.

ACKNOWLEDGMENTS

Authors gratefully acknowledge the extremely valuable work done by Angel Serrano Serrano and Pedro Guerra Cascallana during photo acquisition and survey field work. The authors declare that they don't have any conflict of interest.

FUNDING

This work was supported by Estancias de Movilidad en el Extranjero "José Castillejo" para Jóvenes Doctores (2017), from Ministerio de Educación, Cultura y Deporte, Gobierno de España.

REFERENCES

- Agüera-Vega, F., Carvajal-Ramírez, F., Martínez-Carricando, P., 2017. Assessment of photogrammetric mapping accuracy based on variation ground control points number using unmanned aerial vehicle. *Measurement* 98, 221–227. <https://doi.org/10.1016/j.measurement.2016.12.002>
- Alidoost, F., Arefi, H., 2017. Comparison of UAS-based photogrammetry software for 3D point cloud generation: a survey over a historical site. *ISPRS Ann. Photogramm. Remote Sens. Spat. Inf. Sci. IV-4/W4*, 55–61. <https://doi.org/10.5194/isprs-annals-IV-4-W4-55-2017>
- Barbasiewicz, A., Widerski, T., Daliga, K., 2018. The analysis of the accuracy of spatial models using photogrammetric software: Agisoft Photoscan and Pix4D. Presented at the E3S Web of Conferences. <https://doi.org/10.1051/e3sconf/20182600012>
- Benassi, F., Dall'Asta, E., Diotri, F., Forlani, G., Cella, U.M., Roncella, R., Santise, M., 2017. Testing accuracy and repeatability of UAV blocks oriented with gnss-supported aerial triangulation. *Remote Sens.* 9. <https://doi.org/10.3390/rs9020172>
- Brown, D.C., 1971. Close-range camera calibration. *Photogramm. Eng.* 37, 855–866.
- Burns, J.H.R., Delparte, D., 2017. Comparison of commercial structure-from-motion photogrammetry software used for underwater three-dimensional modeling of coral reef environments. Presented at the International Archives of the Photogrammetry, Remote Sensing and Spatial Information Sciences - ISPRS Archives, pp. 127–131. <https://doi.org/10.5194/isprs-archives-XLII-2-W3-127-2017>
- Carboneau, P.E., Dietrich, J.T., 2017. Cost-effective non-metric photogrammetry from consumer-grade SUAS: implications for direct georeferencing of structure from

- motion photogrammetry. *Earth Surf. Process. Landf.* 42, 473–486.
<https://doi.org/10.1002/esp.4012>
- Cohen, J., 1988. Statistical Power Analysis for the Behavioral Sciences, Edición: 2. ed. Routledge, Hillsdale, N.J.
- Dall'Asta, E., Thoeni, K., Santise, M., Forlani, G., Giacomini, A., Roncella, R., 2015. Network Design and Quality Checks in Automatic Orientation of Close-Range Photogrammetric Blocks. *Sensors* 15, 7985–8008.
<https://doi.org/10.3390/s150407985>
- DeWitt, B.A., Wolf, P.R., 2000. Elements of Photogrammetry (with Applications in GIS), 3rd ed. McGraw-Hill Higher Education.
- Ding, J., Wang, G., Xiong, L., Zhou, X., England, E., 2017. Rapid Topographic Mapping Using TLS and UAV in a Beach-dune-wetland Environment: Case Study in Freeport, Texas, USA. *AGU Fall Meet. Abstr.* 31.
- Eltner, A., Kaiser, A., Castillo, C., Rock, G., Neugirg, F., Abellán, A., 2016. Image-based surface reconstruction in geomorphometry—merits, limits and developments. *Earth Surf. Dyn.* 4, 359–389. <https://doi.org/10.5194/esurf-4-359-2016>
- Eltner, A., Schneider, D., 2015. Analysis of Different Methods for 3D Reconstruction of Natural Surfaces from Parallel-Axes UAV Images. *Photogramm. Rec.* 30, 279–299.
<https://doi.org/10.1111/phor.12115>
- Firdaus, M.I., Rau, J.-Y., 2017. Comparisons of the three-dimensional model reconstructed using MicMac, PIX4D mapper and Photoscan Pro. Presented at the 38th Asian Conference on Remote Sensing - Space Applications: Touching Human Lives, ACRS 2017.
- Fonstad, M.A., Dietrich, J.T., Courville, B.C., Jensen, J.L., Carboneau, P.E., 2013. Topographic structure from motion: a new development in photogrammetric measurement. *Earth Surf. Process. Landf.* 38, 421–430.
<https://doi.org/10.1002/esp.3366>
- Fraser, C., 2018. Camera Calibration Considerations for UAV Photogrammetry, in: Towards Photogrammetry 2020. Presented at the ISPRS Technical Comm. II Symposium 2018, Riva del Garda, Italy. <https://www.isprs.org/tc2-symposium2018/images/ISPRS-Invited-Fraser.pdf>
- Fraser, C.S., Al-Ajlouni, S., 2006. Zoom-dependent camera calibration in digital close-range photogrammetry. *Photogramm. Eng. Remote Sens.* 72, 1017–1026.
<https://doi.org/10.14358/PERS.72.9.1017>
- Fryer, J., Mitchell, H., 1987. Radial Distortion and close-range stereophotogrammetry. *Aust. J. Geod. Photogramm. Surv.* 46 and 47, 123–138.
- Granshaw, S.I., 1980. Bundle Adjustment Methods in Engineering Photogrammetry. *Photogramm. Rec.* 10, 181–207. <https://doi.org/10.1111/j.1477-9730.1980.tb00020.x>
- Grayson, B., Penna, N.T., Mills, J.P., Grant, D.S., 2018. GPS precise point positioning for UAV photogrammetry. *Photogramm. Rec.* 33, 427–447.
<https://doi.org/10.1111/phor.12259>
- Griffiths, D., Burningham, H., 2018. Comparison of pre- and self-calibrated camera calibration models for UAS-derived nadir imagery for a SfM application. *Prog. Phys. Geogr. Earth Environ.* 0309133318788964.
<https://doi.org/10.1177/0309133318788964>
- Harwin, S., Lucieer, A., Osborn, J., 2015. The impact of the calibration method on the accuracy of point clouds derived using unmanned aerial vehicle multi-view stereopsis. *Remote Sens.* 7, 11933–11953. <https://doi.org/10.3390/rs70911933>

- Heikkila, J., Silven, O., 1997. A four-step camera calibration procedure with implicit image correction, in: Proceedings of IEEE Computer Society Conference on Computer Vision and Pattern Recognition. Presented at the Proceedings of IEEE Computer Society Conference on Computer Vision and Pattern Recognition, pp. 1106–1112. <https://doi.org/10.1109/CVPR.1997.609468>
- James, M.R., Robson, S., 2014. Mitigating systematic error in topographic models derived from UAV and ground-based image networks. *Earth Surf. Process. Landf.* 39, 1413–1420. <https://doi.org/10.1002/esp.3609>
- James, M.R., Robson, S., d’Oleire-Oltmanns, S., Niethammer, U., 2017. Optimising UAV topographic surveys processed with structure-from-motion: Ground control quality, quantity and bundle adjustment. *Geomorphology* 280, 51–66. <https://doi.org/10.1016/j.geomorph.2016.11.021>
- Javernick, L., Brasington, J., Caruso, B., 2014. Modeling the topography of shallow braided rivers using Structure-from-Motion photogrammetry. *Geomorphology* 213, 166–182. <https://doi.org/10.1016/j.geomorph.2014.01.006>
- Nesbit, P.R., Hugenholtz, C.H., 2019. Enhancing UAV-SfM 3D model accuracy in high-relief landscapes by incorporating oblique images. *Remote Sens.* 11. <https://doi.org/10.3390/rs11030239>
- Remondino, F., Fraser, C., 2006. Digital camera calibration methods: Considerations and comparisons. Presented at the International Archives of the Photogrammetry, Remote Sensing and Spatial Information Sciences - ISPRS Archives, pp. 266–272.
- Rosnell, T., Honkavaara, E., 2012. Point Cloud Generation from Aerial Image Data Acquired by a Quadrocopter Type Micro Unmanned Aerial Vehicle and a Digital Still Camera. *Sensors* 12, 453–480. <https://doi.org/10.3390/s120100453>
- Sanz-Ablanedo, E., Chandler, J., Rodríguez-Pérez, J., Ordóñez, C., Sanz-Ablanedo, E., Chandler, J.H., Rodríguez-Pérez, J.R., Ordóñez, C., 2018. Accuracy of Unmanned Aerial Vehicle (UAV) and SfM Photogrammetry Survey as a Function of the Number and Location of Ground Control Points Used. *Remote Sens.* 10, 1606. <https://doi.org/10.3390/rs10101606>
- Sanz-Ablanedo, E., Rodríguez-Pérez, J.R., Armesto, J., Taboada, M.F.Á., 2010. Geometric stability and lens decentering in compact digital cameras. *Sensors* 10, 1553–1572. <https://doi.org/10.3390/s100301553>
- Shortis, M.R., Bellman, C.J., Robson, S., Johnston, G.J., Johnson, G.W., 2006. Stability of zoom and fixed lenses used with digital SLR cameras. Presented at the International Archives of the Photogrammetry, Remote Sensing and Spatial Information Sciences - ISPRS Archives, pp. 285–290.
- Smith, M.W., Vericat, D., 2015. From experimental plots to experimental landscapes: Topography, erosion and deposition in sub-humid badlands from Structure-from-Motion photogrammetry. *Earth Surf. Process. Landf.* 40, 1656–1671. <https://doi.org/10.1002/esp.3747>
- Stempfhuber, W., Buchholz, M., 2011. A precise, low-cost rtk gnss system for UAV applications. Presented at the International Archives of the Photogrammetry, Remote Sensing and Spatial Information Sciences - ISPRS Archives, pp. 289–293.
- Turner, D., Lucieer, A., Wallace, L., 2014. Direct Georeferencing of Ultrahigh-Resolution UAV Imagery. *IEEE Trans. Geosci. Remote Sens.* 52, 2738–2745. <https://doi.org/10.1109/TGRS.2013.2265295>
- Turner, D., Lucieer, A., Watson, C., 2012. An automated technique for generating georectified mosaics from ultra-high resolution Unmanned Aerial Vehicle (UAV)

- imagery, based on Structure from Motion (SFM) point clouds. *Remote Sens.* **4**, 1392–1410. <https://doi.org/10.3390/rs4051392>
- Wackrow, R., Chandler, J.H., 2011. Minimising systematic error surfaces in digital elevation models using oblique convergent imagery. *Photogramm. Rec.* **26**, 16–31. <https://doi.org/10.1111/j.1477-9730.2011.00623.x>
- Wackrow, R., Chandler, J.H., 2008. A convergent image configuration for DEM extraction that minimises the systematic effects caused by an inaccurate lens model. *Photogramm. Rec.* **23**, 6–18. <https://doi.org/10.1111/j.1477-9730.2008.00467.x>
- Wang, T., Zeng, J., Liu, D.-J., Yang, L.-Y., 2017. Fast stitching of DOM based on small UAV. *J. Inf. Optim. Sci.* **38**, 1211–1219. <https://doi.org/10.1080/02522667.2017.1367502>
- Woodget, A.S., Carboneau, P.E., Visser, F., Maddock, I.P., 2015. Quantifying submerged fluvial topography using hyperspatial resolution UAS imagery and structure from motion photogrammetry. *Earth Surf. Process. Landf.* **40**, 47–64. <https://doi.org/10.1002/esp.3613>
- Yurtseven, H., 2019. Comparison of GNSS-, TLS- And different altitude UAV-generated datasets on the basis of spatial differences. *ISPRS Int. J. Geo-Inf.* **8**. <https://doi.org/10.3390/ijgi8040175>